A phase inversion strategy for low-tortuosity and ultrahigh-mass-loading nickel-rich layered oxide electrodes

Karanth, Pranav; Weijers, Mark; Ombrini, Pierfrancesco; Ripepi, Davide; Ooms, Frans; Mulder, Fokko M.

DOI
10.1016/j.xcrp.2024.101972

Publication date
2024

Document Version
Final published version

Published in
Cell Reports Physical Science

Citation (APA)
Karanth, P., Weijers, M., Ombrini, P., Ripepi, D., Ooms, F., & Mulder, F. M. (2024). A phase inversion strategy for low-tortuosity and ultrahigh-mass-loading nickel-rich layered oxide electrodes. *Cell Reports Physical Science*, *5*(6), Article 101972. https://doi.org/10.1016/j.xcrp.2024.101972

Cell Reports
Physical Science

CellPress
OPEN ACCESS

Article

A phase inversion strategy for low-tortuosity and ultrahigh-mass-loading nickel-rich layered oxide electrodes

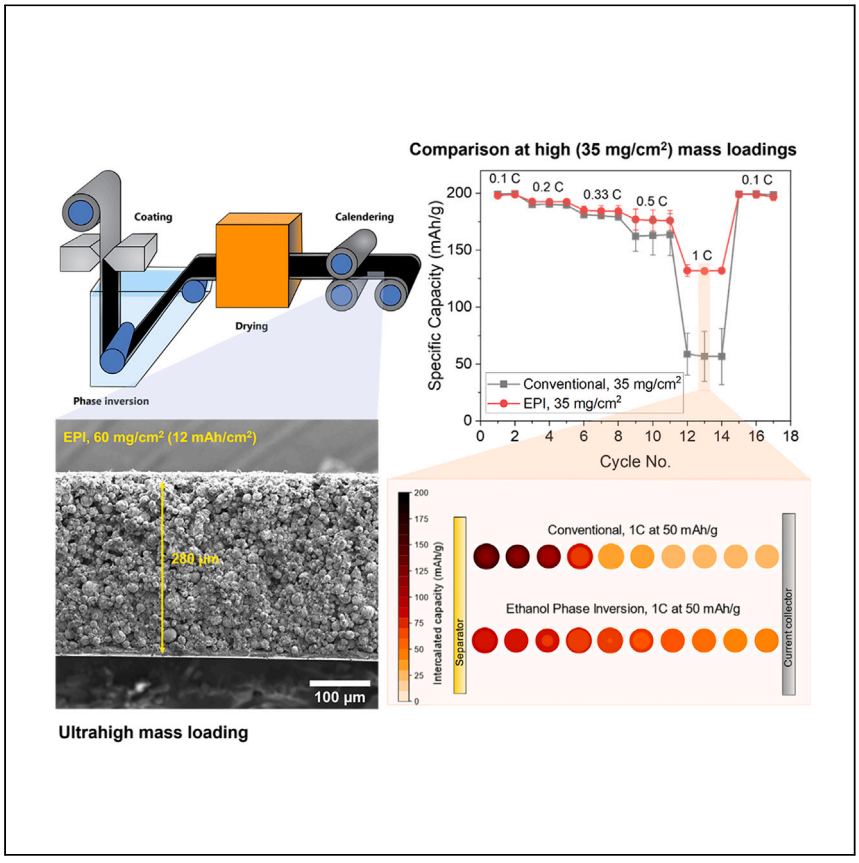

Karanth et al. use ethanol-induced phase inversion to create high-mass-loading, nickel-rich, layered oxide electrodes. The strategy they introduce yields electrodes with improved tortuosity that outperform those fabricated with conventional methods and is expected to be compatible with current roll-to-roll fabrication setups.

Pranav Karanth, Mark Weijers, Pierfrancesco Ombrini, Davide Ripepi, Frans Ooms, Fokko M. Mulder

f.m.mulder@tudelft.nl

Highlights

Ethanol-induced phase inversion is used for high nickel loading in NMC811

Process alters the electrode binder structure, lowering the tortuosity

Rapid binder solidification prevents carbon binder domain migration

Thick electrodes show high capacity retention after 100 cycles at 1C discharge

Karanth et al., Cell Reports Physical Science 5, 101972
June 19, 2024
https://doi.org/10.1016/j.xcrp.2024.101972

Cell Reports
Physical Science

CellPress
OPEN ACCESS

Article

A phase inversion strategy for low-tortuosity and ultrahigh-mass-loading nickel-rich layered oxide electrodes

Pranav Karanth,[1,3] Mark Weijers,[1,3] Pierfrancesco Ombrini,[2] Davide Ripepi,[1] Frans Ooms,[2] and Fokko M. Mulder[1,4,*]

SUMMARY

Increasing the electrode thickness, thereby reducing the proportion of inactive cell components, is one way to achieve higher-energy-density lithium-ion batteries. This, however, results in higher electronic and ionic overpotentials and/or mechanical failure induced by binder migration. Here, we report ethanol-induced phase inversion as an effective method for making high-mass-loading nickel-rich, layered oxide ($LiNi_{0.8}Mn_{0.1}Co_{0.1}O_2$ [NMC811]) electrodes. The ethanol-induced phase inversion electrodes significantly outperform their conventionally processed counterparts with similar loading (35 mg/cm^2) and porosity (30%) in Li/NMC half-cells (131.7 mAh/g vs. 56.7 mAh/g) at 1C (7 mA/cm^2) discharge. The binder structure induced by the nonsolvent improves the pore connectivity and results in lower tortuosity factors. The rapid solvent removal reduces the binder migration during drying, enabling ultrahigh active mass loadings up to 60 mg/cm^2 (12 mAh/cm^2). Further, the compatibility of the phase inversion process with current roll-to-roll coating setups makes this a processing technique with high industrial feasibility.

INTRODUCTION

Increasing the energy density of lithium-ion batteries is a widely researched area today thanks to the ever-increasing demand for higher driving ranges in electric cars[1] and a push for increased adoption of batteries in heavy-duty vehicles such as commercial aircraft.[2,3] A significant part of this research is dedicated to the development of high-energy-density electrodes.[4] From a materials perspective, while a transition to Li metal or Si anodes (from graphite) would significantly boost the pack-level energy densities, Ni-rich layered oxides such as $LiNi_{0.8}Mn_{0.1}Co_{0.1}O_2$ (hereafter referred to as NMC811) remain the active material of choice on the cathode side owing to a combination of factors such as high specific capacity, high intercalation voltage vs. Li (3.6–4.3 V), and good electronic/ionic conductivity. A way to further enhance the cell and pack energy density in terms of electrode architecture, particularly for the cathodes, is increasing the electrode thickness, thereby increasing the active mass loading and reducing the proportion of inactive components (current collectors, casing, etc.).[5]

Increasing the thickness of battery electrodes, however, comes with its own set of technical challenges that can impact the power density and the cycle life of these electrodes. An increase in electrode thickness would increase the path length for the electronic transport through the percolation network (consisting mainly of carbon additives) and the ionic transport through the electrolyte-filled porous

[1]Materials for Energy Conversion and Storage, Department of Chemical Engineering, Delft University of Technology, Building 58, Van der Maasweg 9, 2629 HZ Delft, the Netherlands

[2]Storage of Electrochemical Energy, Department of Radiation Science and Technology, Delft University of Technology, Building 50, Mekelweg 15, 2629 JB Delft, the Netherlands

[3]These authors contributed equally

[4]Lead contact

*Correspondence: f.m.mulder@tudelft.nl

https://doi.org/10.1016/j.xcrp.2024.101972

network.[5] While the former issue can be addressed using 1D and 2D long-range conductive additives,[6,7] ion concentration polarization is generally considered the bigger challenge for thick electrodes, especially when moderate to high charge/discharge rates are desired.[5,8,9]

Ion transport through a porous network is influenced by its porosity and tortuosity factor, which, in turn, affect the MacMullin number; i.e., the ratio of bulk ionic conductivity to effective ionic conductivity of the electrolyte in the porous network.[10] In thick slurry cast electrodes, binder migration toward the separator side, induced by a relatively stronger association of the binder (typically polyvinylidene fluoride [PVDF]) with the solvent (typically NMP) than with the active material, is also reported.[11,12] Binder migration in electrodes would typically result in an unfavorable carbon-binder domain (CBD) and porosity distribution across the depth of the electrode, resulting in higher tortuosity factors.[13] While calendering is an essential step in battery electrode processing, necessary to improve electrical and mechanical contacts, this often negatively affects the electrode tortuosity,[14] particularly in the case of thick electrodes with a nonhomogeneous CBD distribution. Further, the binder migration can also negatively affect the overall mechanical strength of the electrode and its adhesion to the current collector. With the successive electrode volume changes induced over extended cycling periods, both these factors can aggravate contact loss and capacity fade.[15]

Many efforts in the recent past have already focused on developing electrodes with lower tortuosities. The various approaches tried in this regard include freeze casting,[16,17] magnetic alignment,[18–20] laser etching,[21] mold templating,[22,] and reactive templating,[23] among others. However, many of these techniques also result in high electrode porosity and face challenges in terms of scalability. High electrode porosities can be undesirable in the context of volumetric energy density, and it is therefore necessary to develop techniques that can induce lower tortuosities at standard electrode porosities (25%–30%).[24] It is also important to consider the costs involved and the compatibility of the electrode casting technique with the current industrial roll-to-roll processing for battery electrodes.[25]

Nonsolvent-induced phase inversion/separation (also known as NIPS/immersion precipitation), a well-known technique in the membrane processing industry,[26–28] is another such technique that has been used to make high-performance battery electrodes. When the polymer-based (either pure or inorganic/polymer mix) coating makes contact with a binder nonsolvent, liquid-liquid demixing in the metastable region results in a polymer-rich phase (polymer backbone) and a polymer-lean phase (pores).[27,29] Different nonsolvents under different process conditions (temperature, dilution, presence of additives, etc.) result in different demixing rates, which consequently affect the pore connectivity and the pore size distribution.[29,30] In addition to being used for making battery separators, fuel cell electrodes, and flow battery electrodes,[30,31] phase inversion has already been used to produce high-performance sulfur/carbon,[32,33] $Li_4Ti_5O_{12}$,[34] $LiFePO_4$,[34,35] and silicon[36] electrodes for Li-ion batteries, typically using water as the binder nonsolvent. However, to our knowledge, the technique has not yet been applied to state-of-the-art but water-sensitive Ni-rich layered oxide materials (Ni-rich NMC, NCA, LNO, etc.), where a move toward higher mass-loading architectures is of significant interest to enable cell-level-specific energy of 500 Wh/kg and higher.[4]

In this work, we report high-mass-loading, high-rate-performance, Ni-rich NMC811 electrodes prepared using a novel ethanol-induced phase inversion method. The

origin of the improved rate performance for the phase inversion-based electrodes with high active mass loadings (35 mg/cm^2 and higher) is elucidated using a combination of techniques (porosimetry, focused ion beam scanning electron microscopy [FIB-SEM], pseudo-2D (P2D) modeling, symmetric cell electrochemical impedance spectroscopy (EIS), and solid-state NMR). The altered CBD structure for the phase inversion electrodes is shown to significantly reduce the tortuosity factor. Further, stable long-term cycling of the phase inversion electrodes is also observed for these high loadings, demonstrating the potential of phase inversion as a scalable, effective technique to obtain high-mass-loading, Ni-rich, layered oxide electrodes.

RESULTS

Optimization of the phase inversion process for Ni-rich layered oxides

Through the solvent/antisolvent screening for electrode slurries with PVDF as the binder, NMP and DMSO solvents were considered. DMSO is considered a green alternative to the conventionally used NMP[37,38] and is also typically miscible with the nonsolvent of PVDF/NMP. Miscibility of solvent and nonsolvent is necessary to ingress the nonsolvent in the cathode slurry. As opposed to previously investigated battery active materials (such as LFP), where water has often been used as the binder nonsolvent for making phase inversion-based electrodes,[34,35] options for suitable nonsolvents can be more limited for Ni-rich layered oxide materials such as NMC811. NMC811 is alkaline in nature, as it exchanges lithium ions with protons in a protic nonsolvent medium such as water. This Li^+ leaching, leading to the formation of LiOH and Li_2CO_3, and the resulting alkaline environment (pH > 12) subsequently results in corrosion of both the aluminum current collector and the native alumina layer on its surface.[39,40] Also, water phase inversion showed delamination of the electrode from the aluminum current collector after about 15 s, making the manufacturing process more error prone.

The solubility parameters calculated based on the Hansen solubility index[41,42] (Note S1; Table S1) indicate that alcohols are suitable nonsolvents for PVDF. The alcohol hydroxyl group generally has a higher pKa (15.9)[43] compared to the NMC alkalinity measured in an aqueous environment,[39] where relatively more acidic nonsolvents would form lithium salts upon contact. Among alcohols, ethanol was selected owing to its relatively higher abundance, safety, and non-solubility with PVDF. The low enthalpy of evaporation of ethanol, its low viscosity, and ease of separation with NMP and DMSO solvents by extractive distillation[44] or membrane filtration[45] make it a suitable nonsolvent. Also, no delamination from the Al current collector was observed after extended periods of nonsolvent contact.

Further, the choice of dilution decides the viscosity of the slurry and the proximity of the active material particles in the solution during precipitation. The viscosity of DMSO shows a higher dilution dependence and a high temperature dependence (Note S2; Figure S1). NMP slurries show only a slight viscosity difference upon dilution, and only for low dilutions (1:10 PVDF:NMP) is a significant temperature dependence observed. With a 1:10 m:m PVDF:solvent ratio, the electrode height and pore distribution were uneven. Such high viscosities may also not be applicable using conventional slot dye coating processing. A sufficiently low dilution of 1:12 or, ideally, 1:14 m:m PVDF:NMP showed the best distribution in pores (Figure S1). Dilutions up to 1:20 m:m were tried, and too-high dilutions led to a non-binding precipitation. NMP is chosen as the solvent for the rest of this work, as the slurry viscosity shows a smaller temperature and dilution dependence, which improves the repeatability of the experiments.

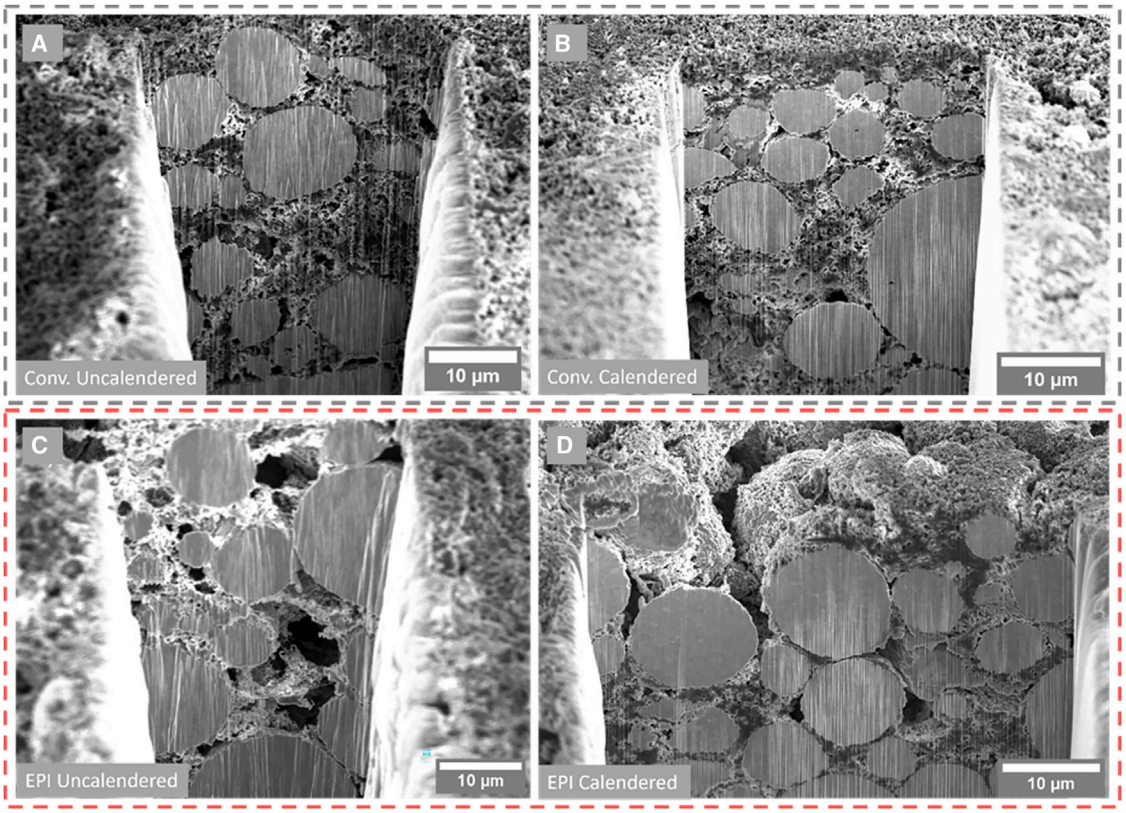

Figure 1. Cross-section FIB-SEM of NMC811 electrodes

(A) Conventional uncalendered.

(B) Conventional calendered.

(C) EPI uncalendered.

(D) EPI calendered.

While the conventional electrodes show a high degree of intra-CBD microporosity before and after calendering (A and B), uncalendered EPI electrodes show a channeled structure with macropores (C). These macropores are retained to some extent with calendering, while the CBD microstructure densifies (D). The length of the scale bars indicates 10 µm.

Changes to the electrode structure upon phase inversion and the effect of calendering

The phase inversion processing of NMC811 electrodes resulted in changes to both the CBD microstructure and the CBD distribution across the depth of the electrode in comparison to the conventional electrodes. Cross-section FIB-SEM images show channel structures throughout the uncalendered ethanol phase inversion (EPI)-based electrodes (Figure 1C), and no significant binder migration is observed (Figure S2C). Further, EPI also causes macropores (pores in the micron range) throughout the cathode material (Figure 1C). Such macropores are not observed in the conventional electrodes. In conventional electrodes, a thick CBD layer is observed on the electrode surface (Figure S2A), and the CBD interconnects the particles with a porous microstructure (Figure 1A). For the EPI electrodes, the rapid precipitation of PVDF upon nonsolvent contact prevents binder migration by causing a rapid polymer-rich phase precipitation, creating a more evenly distributed CB structure throughout the electrode and negligible binder migration.

The immersion time (or solvent/nonsolvent exchange time) optimization also plays a crucial role in the effectiveness of the phase inversion process in generating the

intended binder microstructure, as exchange times less than the binder precipitation time could result in partial/complete reversal of the binder structure generation, making the phase inversion processing ineffective.[46] Here, setting the immersion time to 5 min resulted in a good overall balance in terms of phase inversion/precipitation completeness, electrode adhesion, and overall processing time, resulting in the binder microstructures shown in Figure 1A (cross-section) and Figure S2C (top view). With lower exchange times (1 min), while the binder migration is still reduced in comparison to the conventional electrode (Figure S2A), the CBD still had a porous microstructure similar to the conventional electrodes (Figure S2B), suggesting an incomplete binder precipitation during phase inversion.

For the EPI electrodes, calendering yields an evenly distributed electrode structure, and the macropores between the active material and the CBD phase are partly retained after calendering (Figures 1D and S3). The CBD microstructure becomes denser after calendering for the EPI electrodes, while the conventional electrodes retain a porous CBD microstructure (Figures 1B and S3).

Further, a significant change to the pore size distribution in the electrodes because of phase inversion is observed by mercury intrusion porosimetry (MIP). MIP shows the preferred liquid pathway in the porous structure as a function of applied pressure. Cathode structures before and after calendering (see more details on the target porosity estimation in Note S3) were subjected to MIP to map the changes to the pore size distribution in the CBD phase upon calendering. A cutoff of 10 μm was chosen, as pores larger than this diameter were never observed with microscopy, and mercury intrusion commences first between the cathode sheets. MIP shows a shift in the macropore (pore sizes > 1 μm) size from 1.8 μm for calendered conventional electrodes toward 2.6 μm for calendered EPI electrodes (indicated with lines in Figure 2A). The CBD phase with micropores (pore sizes of 0.1–0.8 μm) is also smaller in the EPI electrodes. This agrees well with the FIB-SEM. The EPI pore size distribution thus shows a lowered CBD porosity and increased macropores, which is beneficial for achieving lower tortuosities in thicker electrodes without affecting the net porosity.

EPI in NMC811 electrodes also results in a change in the degree of crystallinity of PVDF, and this is clearly observed with the ^{19}F MAS NMR measurements (Figures 2C and 2D). For both samples, three environments are observed at −91.2 ppm, 97 ppm, and −114.3 ppm, and these have been previously attributed to the amorphous CH_2-CF_2 component in PVDF, the crystalline CH_2-CF_2 component, and the defect environment (CH_2-CH_2 and CF_2-CF_2 units instead of alternating CH_2-CF_2), respectively.[47] Clearly, a greater extent of the crystalline environment is observed for the electrode that underwent EPI. These results agree well with the FIB-SEM and porosimetry observations that indicate fewer intra-CBD micropores and a denser CBD structure.

The changes to the CBD microstructure and distribution upon EPI were also found to affect the mechanical properties of the EPI NMC811 electrode. In general, for electrodes with 35 mg/cm^2 active mass loading and 30% apparent porosity, the EPI electrodes displayed better flexibility (higher strain tolerance until fracture); i.e., 1.8% in the case of EPI as compared to 0.5% for the conventional electrode (Figure 2B). This could be relevant for roll-to-roll processing of these electrodes and for the application of these electrodes in non-planar cell architectures in which higher electrode flexibility is desired. Further, EPI electrodes at these loadings showed a more uniform adhesion to the Al current collector along the length of the electrode (uniform

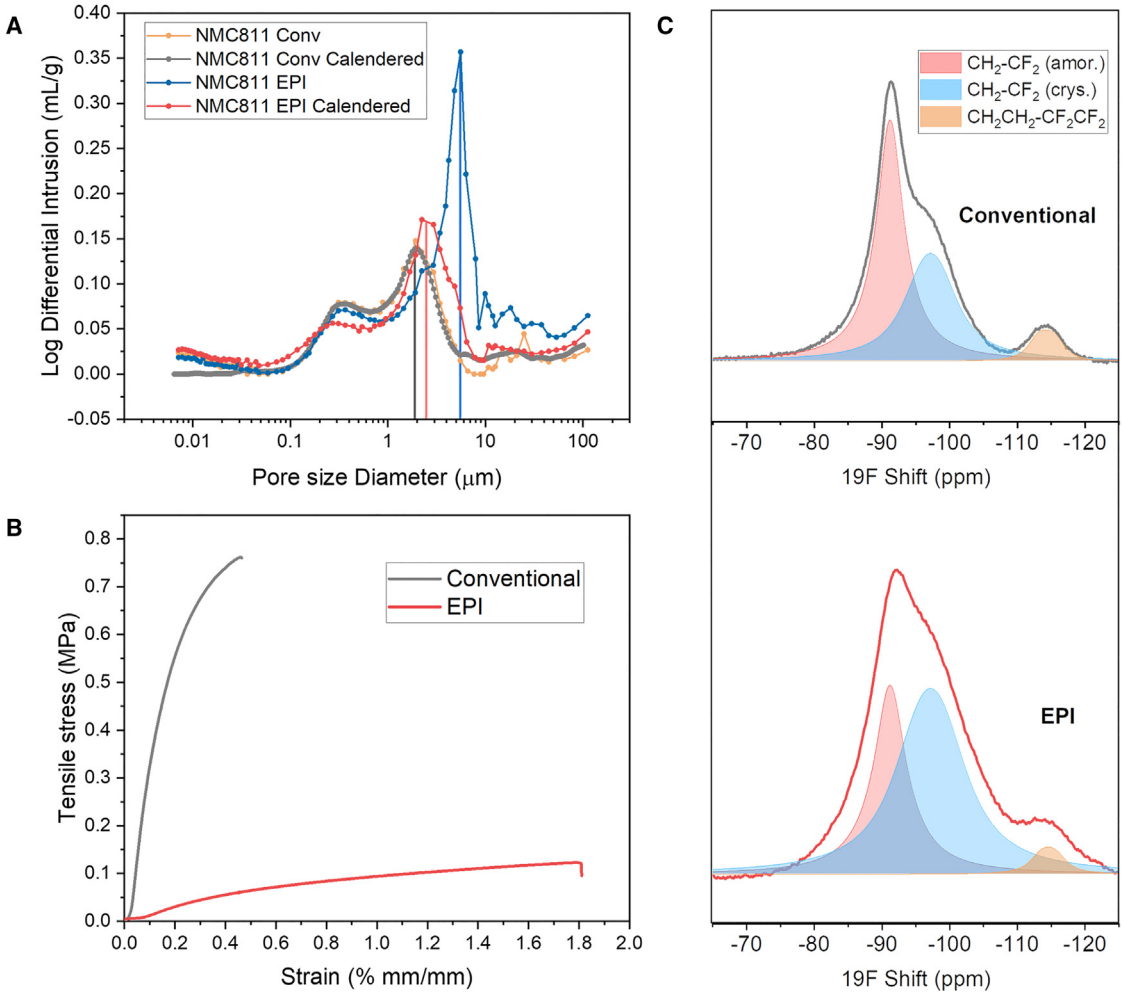

Figure 2. Characterization of NMC811 electrodes

(A) Pore size distribution obtained by MIP of conventional and EPI electrodes before and after calendering.

(B) Tensile stress-strain curves for 35 mg/cm^2, 30% porosity, freestanding conventional and EPI electrodes.

(C) ^{19}F NMR spectra at 32-kHz spinning speed for NMC811 electrodes (4 wt % PVDF) with the conventional drying method (top) and the EPI method (bottom), showing the differences in the amorphous/crystalline CH_2-CF_2 fractions for the two methods.

peeling force) than the conventional electrode (Note S4; Figure S5) at these loadings. These favorable properties for the EPI electrodes enable robust crack-free electrodes at ultrahigh mass loadings of up to 60 mg/cm^2 (280 μm at 30% porosity), while conventional electrodes with a similar loading showed several cracks on the surface (Figure S4).

Differences in electrochemical rate performance

The observed changes to the CBD microstructure in the EPI electrodes are expected to influence the tortuosity of the pore network and the surface coverage (by CBD) of the NMC particles and, thereby, the Li^+ charge transfer resistance. The tortuosity factor of NMC electrodes has been observed previously to be a major bottleneck, particularly at high discharge (lithiation) rates,[14] while any differences in Li^+ charge transfer area would influence both the charge and the discharge rates. In this regard, the NMC811 electrodes were tested for their rate performance under both varying charge and discharge conditions at active mass loadings of 35 mg/cm^2 (7 mAh/cm^2) and apparent porosities of ~30%.

For the varying discharge rate tests, the electrodes were tested up to 1C, with C/10 being the constant charge rate (Figure 3A). For discharge rates up to C/3, not much difference is observed for the discharge capacities. However, higher discharge capacities are observed for the EPI electrode starting from C/2. At 1C, a clear difference in the discharge capacities is observed for the EPI electrodes (131.7 mAh/g vs. 56.7 mAh/g for EPI and Conv. respectively, at cycle 14). From the discharge voltage traces for the two electrodes at 1C (Figure 3B), it can be observed that the ohmic drop during the initial stage of discharge is nearly the same after charging at C/10. During discharge, however, the slope of the discharge curve is lower for the EPI electrode, indicating a lower ionic resistance across the porous electrode network for the EPI electrodes.

In the case of varying charge rate tests (with a C/10 constant discharge rate) shown in Figure 3C, while the discharge capacities remain similar for C/10, higher discharge capacities are observed at C/5 and higher charge rates for the EPI electrodes. At C/2, the EPI electrode shows a discharge capacity of 142 mAh/g as opposed to 88 mAh/g for the conventional electrode. A comparison of the charge/discharge curves of the two electrodes at C/2 charging is shown in Figure 3D. Again, while the ohmic polarization observed for the EPI electrodes is similar to that of the conventional electrodes, a lower slope is observed for the charging curve, corresponding to a higher charge capacity, which could be attributed to higher effective ion migration along the porous electrode network, influenced by the tortuosity factor and/or the porosity, which, in this case, lowers the MacMullin number.

EIS performed on the 35 mg/cm^2 half-cells at 3.7 V after the formation cycles also sheds light on the differences in the impedance contributions for the two electrodes (Figure 3E; see Note S5 for equivalent circuit shown in Figure S6 and fit values in Table S4). The curved features occurring between 500 and 2 kHz, 2 kHz and 50 Hz, and 50 Hz and 1 Hz have been attributed to the total electronic resistance (R_{elec}) of the electrodes (including the contact resistance between the NMC811 electrode film and Al current collector), the Li SEI film resistance (R_{SEI}), and the charge transfer resistance at the cathode-electrolyte interface (R_{CT}), respectively (based on time constants typically reported for these components[48]).

Both electrodes are observed to have similar R_{elec} values perpendicular to the plane, with the value for the EPI cell being slightly lower (12.0 Ω cm^2) compared to the conventional cell (13.1 Ω cm^2). The R_{elec} obtained with EIS is in line with through-plane DC R_{elec} for the electrodes measured in an ion-blocking setup (18.2 Ω cm^2 and 18.4 Ω cm^2 for EPI and conventional electrodes respectively; further details can be found in Note S6 and Table S5). Further, the R_{CT} value for the EPI electrode is observed to be lower (5.50 Ω cm^2) compared to the conventional cell (7.79 Ω cm^2). R_{CT} can depend on several factors, such as the active material, the state of charge, and the available surface area for charge transfer. In this case, the lower R_{CT} in the case of the EPI electrode could be explained by the enhanced surface area for Li^+ exchange, caused by a lower CBD coverage of the active material surface and/or the improved electrolyte uptake in its pore network resulting in a better active surface utilization.

Further, Figure 3F provides an overview of the discharge capacities at different charging currents for NMC811 electrodes at different active mass loadings (17.5–60 mg/cm^2). It can be observed that, while the rate performance of both the conventional and the EPI electrodes is similar for 17.5 mg/cm^2 (3.5 mAh/cm^2), a clear improvement in discharge capacity is observed for the electrodes at 35 mg/cm^2

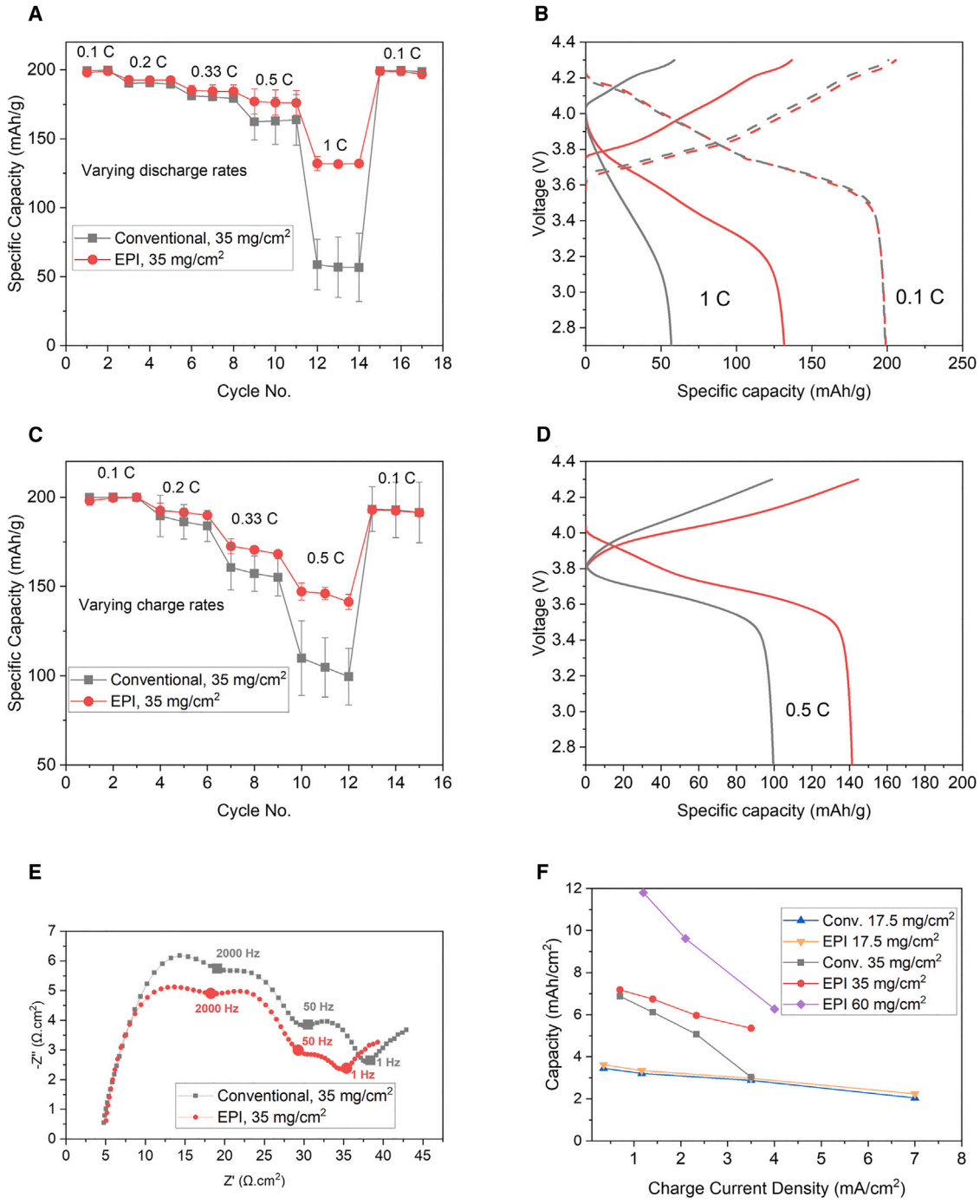

Figure 3. Electrochemical rate performance comparison

(A) Rate performances of 35 mg/cm^2 NMC811 electrodes in Li half-cells at varying discharge rates and a constant C/10 charge rate.

(B) The voltage traces of (A), cycle 13, for both electrodes.

(C) Rate performance of 35 mg/cm^2 NMC811 electrodes in Li half-cells at varying charge rates and a constant C/10 discharge rate.

(D) The voltage traces of (C), cycle 11, for both electrodes.

(E) EIS Nyquist plots at 3.7 V for the conventional and EPI based Li/LP57/NMC811 cells.

(F) Overview of the specific (discharge) capacities for NMC811 electrodes obtained at varying charge rates and mass loadings.

Error bars in (A) and (C) indicate the standard deviation from the mean of a duplicate experiment.

(7 mAh/cm^2), particularly at higher charge rates. EPI electrodes with ultra-high mass loadings of 60 mg/cm^2 (12 mAh/cm^2) also show a remarkable discharge capacity of 9.62 mAh/cm^2 (160.3 mAh/g) capacity at charge current densities of ~2.1 mAh/cm^2, whereas the conventional electrodes cast at these loadings did not show enough mechanical integrity to be tested in coin cells.

Differences in the tortuosity factor

The symmetric cell method EIS (eSCM) measurements for the two electrodes also reveal differences in the ionic resistance contributions from the porous network and the CBD and, therefore, the electrode tortuosity factor. Figures 4A and 4B show the Nyquist plots obtained for the conventional and EPI electrodes.

Both plots show three features; i.e., two curved features in the high-mid-frequency region and a sloping line in the mid-low-frequency region. Similar feature(s) have been observed previously for porous Li-ion electrodes, and their physicochemical interpretation has been subject to much debate. Some possible reasons for such a feature include electrical contact resistance,[49,50] uneven CBD distribution through the depth of the electrode resulting in a depth-wise difference in the ionic resistance,[13,51] and the intrinsic porosity/electrolyte uptake of the CBD.[52]

In this case, the high-frequency feature (up to 6,250 Hz) is attributed to the electronic (contact) resistance of the electrode. The second (mid-frequency) curved feature (6,250–125 Hz) is attributed to the impedances coming from the CBD. The magnitude of this feature is observed to be higher for the EPI electrode than for the conventional one. A possible origin of this feature here could be the non-homogenous distribution of the CBD phase along the depth of the electrode, which is known to occur for thick electrodes with drying. While a migrated binder layer was indeed observed for the conventional electrodes with FIB-SEM, a nonuniform distribution of the CBD was not observable for the EPI electrodes at mass loadings of 7–7.5 mAh/cm^2 (Figure 1A).

When it comes to the CBD structure, however, FIB-SEM (Figure 1C) reveals a more dense CBD structure in terms of microporosity for the EPI electrodes. This observation is also supported by the MIP results (Figure 2A), which show a lower pore size distribution in the 10- to 200-nm range (typically corresponding to intra-CBD pores) and also the 19F ssNMR results (Figures 2C and 2D) that show a more crystalline PVDF structure produced by the EPI process. This results in a lower surface area offered by the CBD phase for the EPI electrodes, explaining the higher real axis value for the second curved feature.

Finally, the sloping line feature occurring at medium to low frequencies denotes the resistance to ion migration through the long-range (macro)porous network along the electrode, and here, the value of ionic resistance appears to be lower for the EPI electrode.

The tortuosity factors are estimated by approximating the sum of the real axis (x axis) lengths of the sloping line and the mid-frequency curve to be $R_{ion}/3$, where R_{ion} is the total ionic resistance of the two electrodes in the symmetric cell.[13,49] This value is then used to calculate the tortuosity factors (further details can be found in Note S7 and Table S6). The EPI electrode displays a lower tortuosity factor of 2.58 compared to a value of 3.79 for the conventional electrode.

The rate performance and the difference in obtainable tortuosity factors for EPI can be further compared to conventional processing through porous electrode modeling.[53–60] The physical constants of the model were found by fitting the

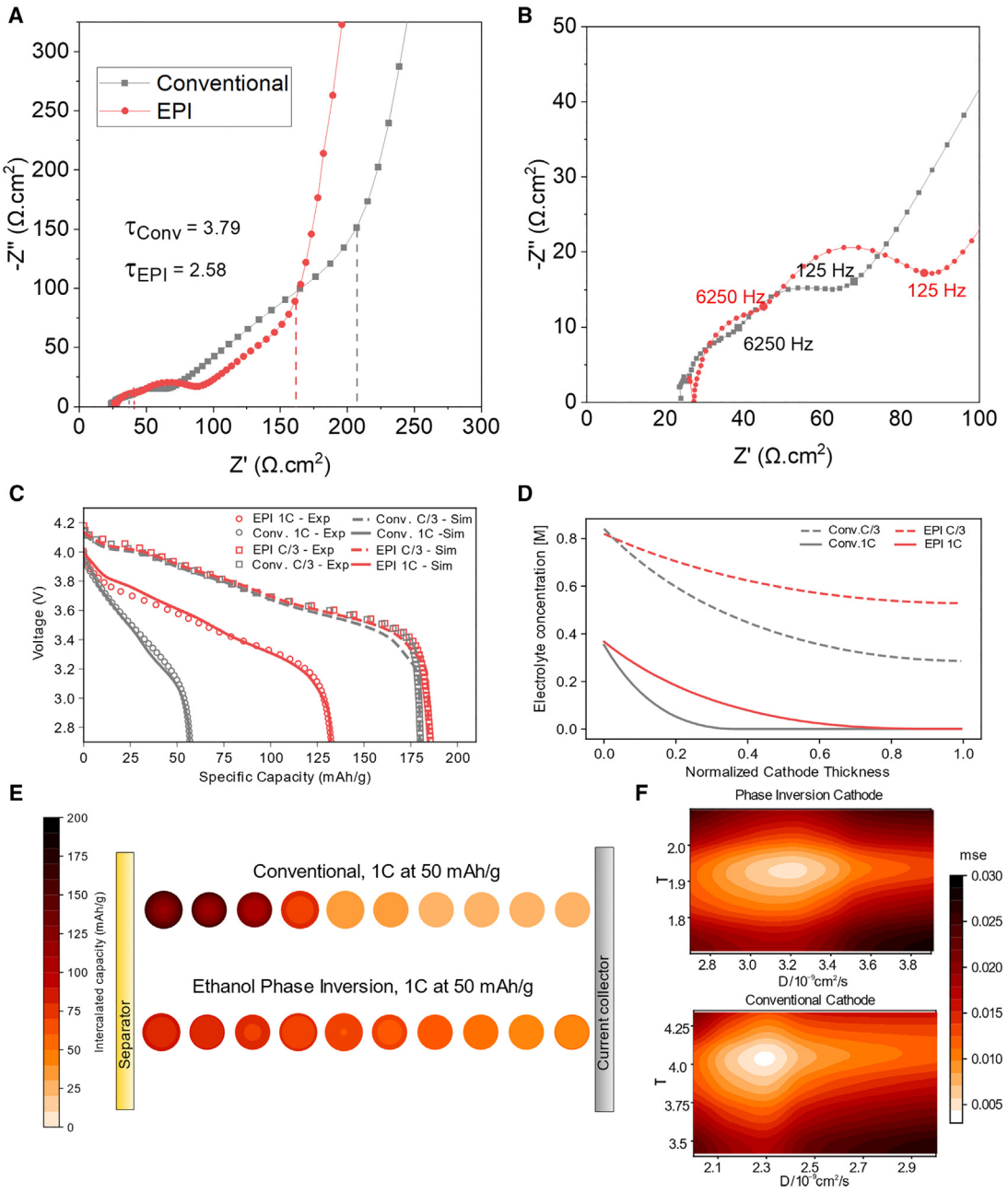

Figure 4. Tortuosity factor measurements

(A) EIS Nyquist plots for the NMC811 symmetric coin cells with 25 mM $TBACIO_4$ in EC:DEC electrolyte. The drop-down values indicate the real axis length considered for the R_{ion} calculations.

(B) Magnification of the high-to-mid frequency region for the NMC811 symmetric cells.

(C) Comparison between the experimental and the simulated voltage curves.

(D) Electrolyte concentration along the cathode at 25% DOD.

(E) Particle concentrations, expressed in terms of capacity delivered during discharge, along the cathode at 25% DOD for conventional and EPI electrodes.

(F) Mse landscape for varying diffusivities (D) and tortuosity factor (τ) for conventional and EPI electrodes.

unknown parameters, such as effective diffusivity, exchange current density, Li metal R_{CT}, and tortuosity factor, to match the experimental voltage curves. The result is shown in Figures 4C–4F.

The effect of the most sensitive parameters (effective diffusivity D and tortuosity factor τ) on the mean square error (mse) between the simulated and the experimental voltage curve (Figure 4F) clarifies the importance of the tortuosity factor in the correct fitting of the experimental results, revealing the best fit for the conventional and the phase inversion to have tortuosity factors of 4.05 and 1.92, respectively.

Despite the intrinsic assumption underlying the P2D model,[61,62] which considers every particle in an ideal electrolyte bath, the relation between the fitted tortuosity factor is in line with the results of the EIS (Figure 4A), showing the effect of the phase inversion on the performance. Moreover, an optimal fit (Figure 4C) is achieved by decreasing the effective diffusivity and the exchange current densities of the conventional electrode compared to the EPI electrode, obtaining values of 2.28 10^{-9} cm^2/s and 3.19 10^{-9} cm^2/s for the effective diffusivities and 2.48 A/m^2 and 3.5 A/m^2 for the exchange current densities, respectively (Note S8). This result, coming from the unbounded parameter estimation, aligns well with the (cathode) R_{CT} calculated from the EIS.

Finally, the validated model shows the effect of the microstructural changes on the Li^+ concentration in the electrolyte along the cathode (Figure 4D), also capturing the consequences in terms of Li concentration in the particles (Figure 4E). This result underlines the advantages of phase inversion in reducing CBD inhomogeneities and the tortuosity factor in thick electrodes.

Long-term cycling performance

A comparison of the long-term electrochemical performances of the conventional and EPI NMC811 electrodes at high active mass loadings of 7 mAh/cm^2 (35 mg/cm^2) is shown in Figure 5. In this case, Li foil (250 μm) was again selected as the anode due to the unavailability of other suitable candidates that can deliver these high capacities without undergoing performance limitations of their own. The electrolyte was changed to a high-entropy salt electrolyte (i.e., 1 M $LiPF_6$ + 0.1 M LiDFOB + 0.1 M LiTFSI + 0.1 M LiFSI + 0.1 M $LiNO_3$ in EC:DMC (1:1 wt %) + 5 wt % FEC (hereafter referred to as 1.4 M HE electrolyte) reported previously by Wang et al.,[63] as high-entropy multi-salt electrolytes have been shown to enable uniform Li plating/stripping at high current density and capacity.[63,64]

Here, a clear improvement in the discharge capacity at 1C is observed for the EPI NMC811 electrode for over 100 cycles (Figure 5A). A gradual capacity fade is observed for both electrodes over the high cycling rates, and such a capacity fade is typically observed due to the increase of polarization at the Li interface due to the buildup of dead Lithium and/or gradual salt consumption at these high plating/stripping rates.[65] This phenomenon contributes to the increase of ohmic polarization during charge, going from cycle 4 to 104 for both electrodes (Figures 5B and 5C). However, the original capacities are observed to be nearly retained for both electrodes at low rates (0.1 C) after the 100 cycles. Remarkably, the EPI electrodes show a capacity retention of 98.65% (197.3 mAh/g) even after cycling with significantly higher discharge capacities compared to the conventional electrodes for over 100 cycles.

DISCUSSION

EPI processing on casted NMC811 slurries causes rapid precipitation of the CBD. As the nonsolvent enters, the low miscibility of the binder with the solvent/nonsolvent phase results in the formation of a polymer-rich phase in the solution and subsequent precipitation of the binder. The solvent/nonsolvent phase penetrates throughout the electrode, solidifying the constituents of the final electrode.

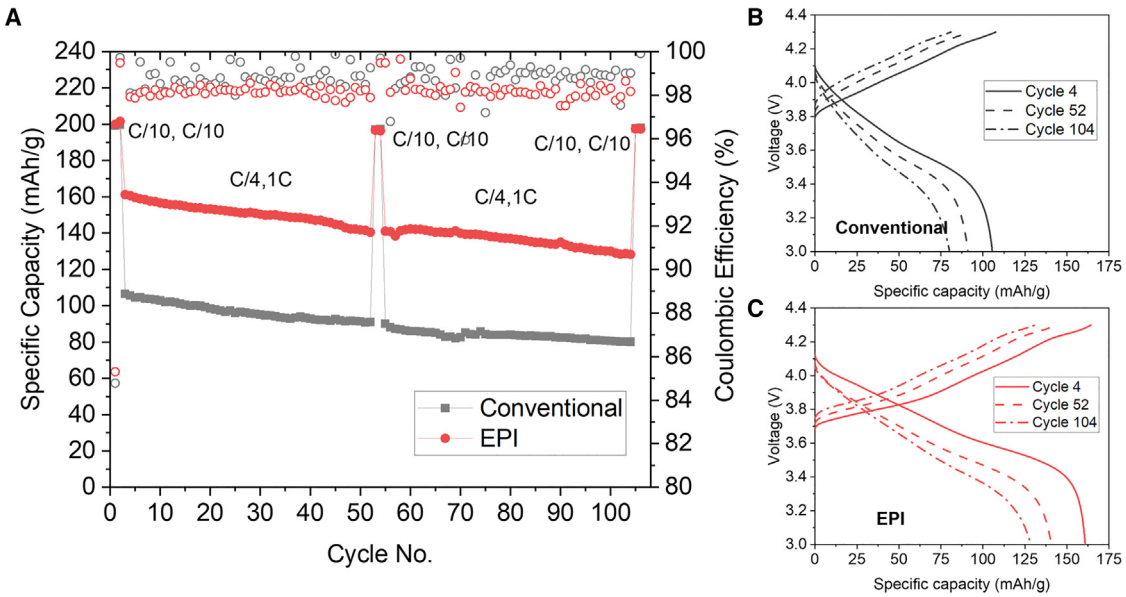

Figure 5. Long-term cycling comparison

(A) Discharge capacities and Coulombic efficiencies in Li/NMC811 half-cells with 35 mg/cm^2 (7 mAh/cm^2) active mass loading and 1.4 M HE electrolyte cycled at 20°C.

(B) Voltage traces for the conventional Li/NMC811 cells at 10, 52, and 104 cycles.

(C) Voltage traces for the EPI Li/NMC811 cells at 4, 52, and 104 cycles (C/4 C, 1C D).

As a result, phase inversion processing shows a substantial change in the CBD phase (Figure 6B), as shown with FIB-SEM, MIP, and solid-state NMR. The rapid precipitation of the binder with EPI results in electrodes with a higher degree of (connected) macropores but a lower degree of micropores, even after calendering (Figure 6B). The reduction in the degree of microporosity for the EPI electrodes was also further confirmed by ^{19}F NMR, which shows a higher degree of PVDF crystallinity, increasing the overall volumetric density of the PVDF binder. The FIB-SEM also reveals a reduction in the degree of binder migration for the EPI NMC811 electrodes.

The EPI electrodes show an improved flexibility, essential for roll-to-roll processing of thick electrode architectures. The structure maintains its integrity during calendering and results in electrodes with improved rate performance at both high charge and discharge rates.

The eSCM (EIS) using a non-intercalating electrolyte showed a significant decrease in tortuosity factor for the EPI electrodes. The lower tortuosity results in a higher charge capacity at high charge rates, but the capacity gain is more evident during high discharge. During fast discharge, Li^+ concentration depletion due to insufficient influx in a tortuous pore network causes uneven charge distribution across the depth of the electrode and a rapid (concentration) overpotential buildup. In this regard, a lower tortuosity of the pore network is beneficial for maintaining sufficient ion flux deeper in the cathode. The effect of tortuosity is shown using the P2D model, and the computed tortuosity factors nearly match the experimental values for both conventional and phase inversion electrodes.

The EPI electrodes consistently maintain a higher discharge capacity over 100+ cycles during long-term cycling tests of high mass loading (35 mg/cm^2). While both EPI and conventional electrodes show the same gradual capacity fade mechanism at

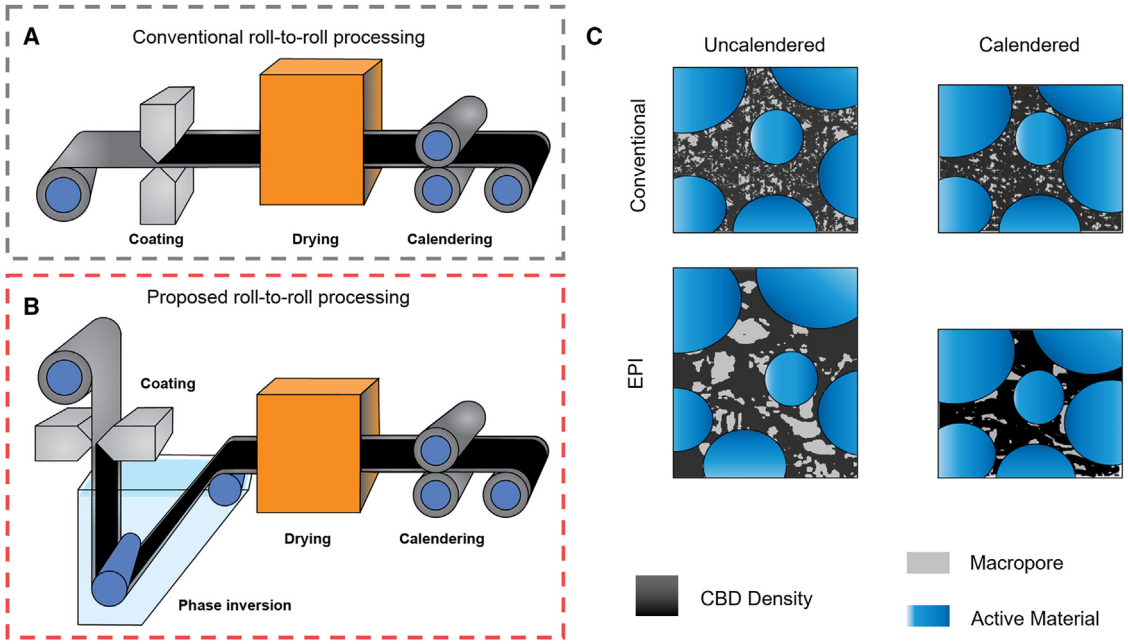

Figure 6. Differences between conventional and EPI processes

(A) Schematic of the current roll-to-roll process based on conventional drying.

(B) Schematic of the proposed roll-to-roll process based on phase inversion.

(C) Electrode microstructures obtained before and after calendering for the conventional and EPI processes.

high discharge rates (1C, 7 mA/cm^2) originating from the increase in impedance from the Li metal anode, the EPI electrode shows an excellent capacity retention of 98.65%.

Estimates of the cell-level volumetric and weight density of batteries fitted with double-sided EPI electrodes shown in this work are 1,210 Wh/L and 503 Wh/kg, respectively, without casing. Here, the calculation assumes a zero-excess lithium configuration and Celgard separators filled with conventional liquid electrolyte (Note S9; Table S8). For lithium excess architectures, using twice the lithium inventory needed for the rated capacity, the energy density will slightly lower to 1,054 Wh/L and 487 Wh/kg. These values highlight the benefit of high mass loadings enabled by EPI, as the inactive components in a cell lower from 43% to 37% of the total cell when going from 4 to 7 mAh/cm^2.

To implement phase inversion processing in current industrial practice, the conventional roll-to-roll electrode manufacturing setup would need an additional nonsolvent processing step. As typical solvents are replaced with more volatile and/or benign nonsolvents, introducing phase inversion would lower the energy investment of subsequent drying and ease solvent recovery. In this work and previous studies,[30–36] it is shown that phase inversion processing is compatible with a wide range of materials and compositions. Finally, the available literature on membrane processing using phase inversion steps allows a steep learning curve in a roll-to-roll setup.

In summary, we developed a new EPI-based strategy for making ultrahigh-loading, high-performance electrodes out of Ni-rich layered oxide materials. We show high active mass loading (35 mg/cm^2) EPI NMC811 electrodes that outperform conventional NMC811 electrodes during fast charge (50% improvement at 0.5C) and

discharge (120% improvement at 1C) at similar porosities (~30%). Unlike conventional electrodes, EPI electrodes can be made ultrathick (60 mg/cm^2, 12 mAh/cm^2) without delamination or cracking issues. The EPI electrodes show a higher gravimetric capacity and similar capacity retention as the conventional electrodes on extensive cycling, which indicates that the processing does not adversely affect the cathode active material. The improved rate performance originates from the lower tortuosity of the electrode. With the addition of a phase inversion processing step in conventional battery manufacturing processes, it is possible to increase the rate performance of battery electrodes at high mass loadings, and this presents a viable path toward future batteries with both high energy and power densities.

EXPERIMENTAL PROCEDURES

Resource availability

Lead contact

Requests for further information and resources should be directed to and will be provided by the lead contact, Fokko Mulder (f.m.mulder@tudelft.nl).

Materials availability

This study did not generate new materials.

Data and code availability

The code developed for this work is based on the open-source MPET model, of which a branch specific to this work is available at https://doi.org/10.5281/zenodo.10932567. The datasets that support the findings of this study are available from the lead contact upon reasonable request.

Electrode manufacturing

NMC811 electrodes were made with a 92:4:3:1 mass ratio of active material (AM): binder:carbon black:graphite using a dry and wet mixing step. First, NMC811 (Umicore) AM was mixed with the conductive additive carbon black C45 (Imerys) in a mortar, followed by the addition and mixing of KS4 graphite (Imerys) and Solef 5130 (Solvay) PVDF, respectively. NMP (Sigma-Aldrich) was added to this mixture at a 1:14 PVDF:NMP mass ratio, and subsequently, the suspension was mixed using a high-shear top stirrer (IKA Microstar 7.5) for 1 h at 1,000 rpm to create a homogeneous slurry. The obtained slurry was cast on aluminum foil using a doctor blade. To obtain freestanding electrodes for the purpose of tensile strength and MIP measurements, the slurry was cast on clean glass plates. Immediately after casting, the sheet was either immersed in a bath of ethanol (96%, VWR) for 60–300 s (EPI) or not subjected to an immersion treatment (conventional). The electrode sheets were dried in two steps. NMP/nonsolvent was evaporated in an oven at 70°C for an hour, and subsequently, the electrode sheets were dried in a vacuum oven at 60°C for 24 h. Finally, the electrodes were calendered to 30% apparent porosity using a calender press (MTI). Details regarding the porosity estimation are provided in Tables S2 and S3).

Electrode characterization

Electrode porosity and pore size distribution of freestanding NMC811 electrodes were tested using MIP (Autopore 9500, Micromeritics). Approximately 1 g of freestanding electrode sample was loaded in strips of 3 × 1 cm in a 15-mL penetrometer with the surface perpendicular to the entry side of the mercury. A stem volume of 0.39 mL was utilized between 40% and 88% during pressurization between 3.7 kPa and 210 MPa. Rheometry was performed on the slurries using a 40-mm Peltier plate with a 0° cone angle and 500 μm gap width on a Discovery HR10 rheometer (TA Instruments). The shear rate varied between 0.01 and 10/s.

SEM pictures were taken using a JEOL JSM-IT700HR FE-SEM setup either in scattering electron imaging (Acc. voltage, 1–5 kV) or backscattered electron imaging (Acc. voltage, 5 kV) mode. FIB-SEM images were taken using a Helios G4 CX. Ion milling times were referenced to 0.8 times the silicon etching duration for a specific depth. The ion beam was set to 30 kV with 65-nA beam strength.

Solid-state magic angle spinning (MAS) NMR measurements were carried out on a Bruker Avance 500 spectrometer. NMC811 electrodes coated on Al foil were scraped off and packed into 1.9-mm rotors. ^{19}F NMR (Larmor frequency, 475 MHz) was carried out at 32 kHz spinning speeds. A background subtraction (zgbs) protocol was used with a recycle delay of 2 s. All spectra were processed and fitted using Mestrenova 14 software.

The tensile strength measurements were performed on a ZwickRoell 10-kN universal testing machine. For these measurements, freestanding electrodes were calendered between two Ni foils to a porosity of 30% and cut according to ASTMD412 type F,[66] with the target test area being about 6 × 50 mm. The tensile force test was performed at a speed of 1 mm/min.

Electrochemical characterization

Coin cells (CR2032) were assembled to study the rate performance of the NMC811 electrodes in a half-cell configuration. NMC811 electrodes were punched as 12.7-mm discs and assembled versus a 250-μm lithium disc (Tobmachine) in an argon-filled glove box. One Celgard 2400 and one Whatman separator (grade Gf/C) each were used, with 110 μL of 1 M $LiPF_6$ in 3:7 EC:EMC (vol %) electrolyte (LP57, ELyte) per cell. After 24 h of rest, the cells underwent two formation cycles at C/10 on a Maccor 3400 galvanostat. Rate performance tests were then carried out on the Maccor 3400 at 20°C.

The long-term cycling performance of the NMC811 electrodes was also tested similarly in a half-cell configuration (vs. Li), except that the electrolyte used was changed to 1 M $LiPF_6$ + 0.1 M LiDFOB + 0.1 M LiTFSI + 0.1 M LiFSI + 0.1 M $LiNO_3$ in EC:DMC (1:1 wt %) + 5 wt % FEC (1.4 M HE) for the sake of improved long-term stability with the Li metal anode at high plating and stripping currents. The 1.4 M HE electrolyte was prepared as described elsewhere.[63] The long-term cycling was carried out at 20°C. Following the formation cycles at C/10, the protocol used was as follows: first 2 cycles at C/10 charge-discharge, followed by 50 cycles at C/4 charge and 1C discharge, and the protocol was repeated every 52 cycles.

EIS was performed on a potentiostat (Metrohm Autolab) after the formation cycles. First, a voltage hold (until I < 0.01C) at 3.7 V was carried out. A frequency range from 500 kHz to 100 mHz was used. The analysis and fitting of the spectra was carried out using Zview (Scribner). Tortuosity factors were measured for these electrodes based on the symmetric cell method often applied to Li-ion battery electrodes.[49,67] A non-intercalating electrolyte, 25 mM $TBAClO_4$ in EC:DEC (1:1 vol %), was used, along with fully intercalated NMC811 electrodes of interest, to achieve the desired blocking conditions for ion flow. Both electrodes had mass loadings around 7.5 mAh/cm^2 and were calendered to an apparent porosity of 30%.

P2D modeling

Simulations were carried out using the open-source software MPET,[68] which uses a standard P2D model.[60,69] The parameters (Table S7) were obtained as follows. The electrolyte parameters for the Stefan-Maxwell model[70] were obtained from the work of Nyman

et al.[71] The dependence on the concentration of the reaction resistivity and the solid-state diffusivity were taken from the fitting of McClelland et al.[72] Electrical conductivity, thickness, porosity, and particle size distribution were taken from measured values. The rest of the parameters, such as the tortuosity factor, were estimated by minimization of the weighted mse. The details of the model can be found in Note S8.

SUPPLEMENTAL INFORMATION

Supplemental information can be found online at https://doi.org/10.1016/j.xcrp.2024.101972.

ACKNOWLEDGMENTS

This project has received funding from the European Union's Horizon 2020 Research and Innovation Program under grant agreement 875557. Neither the European Commission nor any person acting on behalf of the Commission is responsible for how the following information is used. The views expressed in this publication are the sole responsibility of the authors and do not necessarily reflect the views of the European Commission. The authors would like to acknowledge Microlab, Kavli Lab, and DASML (all TU Delft) for using their Mercury Intrusion Porosimetry FIB-SEM and Tensile Strength setups, respectively.

AUTHOR CONTRIBUTIONS

P.K., conceptualization, investigation, methodology, validation, and writing – original draft; M.W., conceptualization, investigation, methodology, validation, and writing – original draft; P.O., investigation, methodology, validation, and writing – original draft; D.R., investigation, methodology, and validation; F.O., Methodology, project administration, resources, and supervision; F.M., conceptualization, formal analysis, funding acquisition, project administration, supervision, and writing – review & editing.

DECLARATION OF INTERESTS

The authors declare no conflict of interest.

Received: October 29, 2023
Revised: February 15, 2024
Accepted: April 18, 2024
Published: May 9, 2024

REFERENCES

1. Masias, A., Marcicki, J., and Paxton, W.A. (2021). Opportunities and Challenges of Lithium Ion Batteries in Automotive Applications. ACS Energy Lett. *6*, 621–630. https://doi.org/10.1021/acsenergylett.0c02584.

2. Viswanathan, V., Epstein, A.H., Chiang, Y.-M., Takeuchi, E., Bradley, M., Langford, J., and Winter, M. (2022). The challenges and opportunities of battery-powered flight. Nature *601*, 519–525. https://doi.org/10.1038/s41586-021-04139-1.

3. Bills, A., Sripad, S., Fredericks, W.L., Singh, M., and Viswanathan, V. (2020). Performance Metrics Required of Next-Generation Batteries to Electrify Commercial Aircraft. ACS Energy Lett. *5*, 663–668. https://doi.org/10.1021/acsenergylett.9b02574.

4. Liu, J., Bao, Z., Cui, Y., Dufek, E.J., Goodenough, J.B., Khalifah, P., Li, Q., Liaw, B.Y., Liu, P., Manthiram, A., et al. (2019). Pathways for practical high-energy long-cycling lithium metal batteries. Nat. Energy *4*, 180–186. https://doi.org/10.1038/s41560-019-0338-x.

5. Kuang, Y., Chen, C., Kirsch, D., and Hu, L. (2019). Thick Electrode Batteries: Principles, Opportunities, and Challenges. Adv. Energy Mater. *9*, 1901457. https://doi.org/10.1002/aenm.201901457.

6. Park, S.-H., King, P.J., Tian, R., Boland, C.S., Coelho, J., Zhang, C.J., McBean, P., McEvoy, N., Kremer, M.P., Daly, D., et al. (2019). High areal capacity battery electrodes enabled by segregated nanotube networks. Nat. Energy *4*, 560–567. https://doi.org/10.1038/s41560-019-0398-y.

7. Yao, W., Chouchane, M., Li, W., Bai, S., Liu, Z., Li, L., Chen, A.X., Sayahpour, B., Shimizu, R., Raghavendran, G., et al. (2023). A 5 V-class cobalt-free battery cathode with high loading enabled by dry coating. Energy Environ. Sci. *16*, 1620–1630. https://doi.org/10.1039/D2EE03840D.

8. Gao, H., Wu, Q., Hu, Y., Zheng, J.P., Amine, K., and Chen, Z. (2018). Revealing the Rate-Limiting Li-Ion Diffusion Pathway in Ultrathick Electrodes for Li-Ion Batteries. J. Phys. Chem. Lett. *9*, 5100–5104. https://doi.org/10.1021/acs.jpclett.8b02229.

9. Weiss, M., Ruess, R., Kasnatscheew, J., Levartovsky, Y., Levy, N.R., Minnmann, P., Stolz, L., Waldmann, T., Wohlfahrt-Mehrens, M., Aurbach, D., et al. (2021). Fast Charging of Lithium-Ion Batteries: A Review of Materials

Aspects. Adv. Energy Mater. *11*, 2101126. https://doi.org/10.1002/aenm.202101126.

10. Tjaden, B., Brett, D.J.L., and Shearing, P.R. (2018). Tortuosity in electrochemical devices: a review of calculation approaches. Int. Mater. Rev. *63*, 47–67. https://doi.org/10.1080/09506608.2016.1249995.

11. Kremer, L.S., Hoffmann, A., Danner, T., Hein, S., Prifling, B., Westhoff, D., Dreer, C., Latz, A., Schmidt, V., and Wohlfahrt-Mehrens, M. (2020). Manufacturing Process for Improved Ultra-Thick Cathodes in High-Energy Lithium-Ion Batteries. Energ. Tech. *8*, 1900167. https://doi.org/10.1002/ente.201900167.

12. Jaiser, S., Müller, M., Baunach, M., Bauer, W., Scharfer, P., and Schabel, W. (2016). Investigation of film solidification and binder migration during drying of Li-Ion battery anodes. J. Power Sources *318*, 210–219. https://doi.org/10.1016/j.jpowsour.2016.04.018.

13. Nguyen, T.-T., Demortière, A., Fleutot, B., Delobel, B., Delacourt, C., and Cooper, S.J. (2020). The electrode tortuosity factor: why the conventional tortuosity factor is not well suited for quantifying transport in porous Li-ion battery electrodes and what to use instead. npj Comput. Mater. *6*, 123. https://doi.org/10.1038/s41524-020-00386-4.

14. Lu, X., Daemi, S.R., Bertei, A., Kok, M.D., O'Regan, K.B., Rasha, L., Park, J., Hinds, G., Kendrick, E., Brett, D.J., and Shearing, P.R. (2020). Microstructural Evolution of Battery Electrodes During Calendering. Joule *4*, 2746–2768. https://doi.org/10.1016/j.joule.2020.10.010.

15. Xu, R., Yang, Y., Yin, F., Liu, P., Cloetens, P., Liu, Y., Lin, F., and Zhao, K. (2019). Heterogeneous damage in Li-ion batteries: Experimental analysis and theoretical modeling. J. Mech. Phys. Solid. *129*, 160–183. https://doi.org/10.1016/j.jmps.2019.05.003.

16. Huang, C., Leung, C.L.A., Leung, P., and Grant, P.S. (2021). A Solid-State Battery Cathode with a Polymer Composite Electrolyte and Low Tortuosity Microstructure by Directional Freezing and Polymerization. Adv. Energy Mater. *11*, 2002387. https://doi.org/10.1002/aenm.202002387.

17. Delattre, B., Amin, R., Sander, J., De Coninck, J., Tomsia, A.P., and Chiang, Y.-M. (2018). Impact of Pore Tortuosity on Electrode Kinetics in Lithium Battery Electrodes: Study in Directionally Freeze-Cast LiNi0.8Co0.15Al0.05O2 (NCA). J. Electrochem. Soc. *165*, A388–A395. https://doi.org/10.1149/2.1321802jes.

18. Billaud, J., Bouville, F., Magrini, T., Villevieille, C., and Studart, A.R. (2016). Magnetically aligned graphite electrodes for high-rate performance Li-ion batteries. Nat. Energy *1*, 16097–16106. https://doi.org/10.1038/nenergy.2016.97.

19. Li, L., Erb, R.M., Wang, J., Wang, J., and Chiang, Y.-M. (2019). Fabrication of Low-Tortuosity Ultrahigh-Area-Capacity Battery Electrodes through Magnetic Alignment of Emulsion-Based Slurries. Adv. Energy Mater. *9*, 1802472. https://doi.org/10.1002/aenm.201802472.

20. Sander, J.S., Erb, R.M., Li, L., Gurijala, A., and Chiang, Y.-M. (2016). High-performance battery electrodes via magnetic templating. Nat. Energy *1*, 16099. https://doi.org/10.1038/nenergy.2016.99.

21. Chen, K.-H., Namkoong, M.J., Goel, V., Yang, C., Kazemiabnavi, S., Mortuza, S.M., Kazyak, E., Mazumder, J., Thornton, K., Sakamoto, J., and Dasgupta, N.P. (2020). Efficient fast-charging of lithium-ion batteries enabled by laser-patterned three-dimensional graphite anode architectures. J. Power Sources *471*, 228475. https://doi.org/10.1016/j.jpowsour.2020.228475.

22. Singh, D.P., George, A., Kumar, R.V., ten Elshof, J.E., and Wagemaker, M. (2013). Nanostructured TiO2 Anatase Micropatterned Three-Dimensional Electrodes for High-Performance Li-Ion Batteries. J. Phys. Chem. C *117*, 19809–19815. https://doi.org/10.1021/jp3118659.

23. Singh, D.P., Mulder, F.M., Abdelkader, A.M., and Wagemaker, M. (2013). Facile Micro Templating LiFePO4 Electrodes for High Performance Li-Ion Batteries. Adv. Energy Mater. *3*, 572–578. https://doi.org/10.1002/aenm.201200704.

24. Boyce, A.M., Cumming, D.J., Huang, C., Zankowski, S.P., Grant, P.S., Brett, D.J.L., and Shearing, P.R. (2021). Design of Scalable, Next-Generation Thick Electrodes: Opportunities and Challenges. ACS Nano *15*, 18624–18632. https://doi.org/10.1021/acsnano.1c09687.

25. Kwade, A., Haselrieder, W., Leithoff, R., Modlinger, A., Dietrich, F., and Droeder, K. (2018). Current status and challenges for automotive battery production technologies. Nat. Energy *3*, 290–300. https://doi.org/10.1038/s41560-018-0130-3.

26. Kingsbury, B.F., and Li, K. (2009). A morphological study of ceramic hollow fibre membranes. J. Membr. Sci. *328*, 134–140. https://doi.org/10.1016/j.memsci.2008.11.050.

27. van de Witte, P., Dijkstra, P.J., van den Berg, J.W.A., and Feijen, J. (1996). Phase separation processes in polymer solutions in relation to membrane formation. J. Membr. Sci. *117*, 1–31. https://doi.org/10.1016/0376-7388(96)00088-9.

28. Lee, M., Wang, B., Wu, Z., and Li, K. (2015). Formation of micro-channels in ceramic membranes – Spatial structure, simulation, and potential use in water treatment. J. Membr. Sci. *483*, 1–14. https://doi.org/10.1016/j.memsci.2015.02.023.

29. Hołda, A.K., and Vankelecom, I.F. (2015). Understanding and guiding the phase inversion process for synthesis of solvent resistant nanofiltration membranes. J. Appl. Polym. Sci. *132*. https://doi.org/10.1002/app.42130.

30. Jacquemond, R.R., Wan, C.T.-C., Chiang, Y.-M., Borneman, Z., Brushett, F.R., Nijmeijer, K., and Forner-Cuenca, A. (2022). Microstructural engineering of high-power redox flow battery electrodes via non-solvent induced phase separation. Cell Rep. Phys. Sci. *3*, 100943. https://doi.org/10.1016/j.xcrp.2022.100943.

31. Wan, C.T.-C., Jacquemond, R.R., Chiang, Y.-M., Nijmeijer, K., Brushett, F.R., and Forner-Cuenca, A. (2021). Non-Solvent Induced Phase Separation Enables Designer Redox Flow Battery Electrodes. Adv. Mater. *33*, 2006716. https://doi.org/10.1002/adma.202006716.

32. Yang, X., Chen, Y., Wang, M., Zhang, H., Li, X., and Zhang, H. (2016). Phase Inversion: A Universal Method to Create High-Performance Porous Electrodes for Nanoparticle-Based Energy Storage Devices. Adv. Funct. Mater. *26*, 8427–8434. https://doi.org/10.1002/adfm.201604229.

33. Wahyudi, W., Cao, Z., Kumar, P., Li, M., Wu, Y., Hedhili, M.N., Anthopoulos, T.D., Cavallo, L., Li, L.-J., and Ming, J. (2018). Phase Inversion Strategy to Flexible Freestanding Electrode: Critical Coupling of Binders and Electrolytes for High Performance Li–S Battery. Adv. Funct. Mater. *28*, 1802244. https://doi.org/10.1002/adfm.201802244.

34. Harks, P.P.R., Robledo, C.B., George, C., Wang, C., van Dijk, T., Sturkenboom, L., Roesink, E.D., and Mulder, F.M. (2019). Immersion precipitation route towards high performance thick and flexible electrodes for Li-ion batteries. J. Power Sources *441*, 227200. https://doi.org/10.1016/j.jpowsour.2019.227200.

35. Wu, J., Ju, Z., Zhang, X., Quilty, C., Takeuchi, K.J., Bock, D.C., Marschilok, A.C., Takeuchi, E.S., and Yu, G. (2021). Ultrahigh-Capacity and Scalable Architected Battery Electrodes via Tortuosity Modulation. ACS Nano *15*, 19109–19118. https://doi.org/10.1021/acsnano.1c06491.

36. Jimenez, N.P., Balogh, M.P., and Halalay, I.C. (2021). High Porosity Single-Phase Silicon Negative Electrode Made with Phase-Inversion. J. Electrochem. Soc. *168*, 040507. https://doi.org/10.1149/1945-7111/abe3f1.

37. Evenepoel, N., Wen, S., Tilahun Tsehaye, M., and Van der Bruggen, B. (2018). Potential of DMSO as greener solvent for PES ultra- and nanofiltration membrane preparation. J. Appl. Polym. Sci. *135*, 46494. https://doi.org/10.1002/app.46494.

38. Wang, M., Dong, X., Escobar, I.C., and Cheng, Y.-T. (2020). Lithium Ion Battery Electrodes Made Using Dimethyl Sulfoxide (DMSO)—A Green Solvent. ACS Sustain. Chem. Eng. *8*, 11046–11051. https://doi.org/10.1021/acssuschemeng.0c02884.

39. Li, S.Y., and Church, B.C. (2016). Effect of aqueous-based cathode slurry pH and immersion time on corrosion of aluminum current collector in lithium-ion batteries. Mater. Corros. *67*, 978–987. https://doi.org/10.1002/maco.201608843.

40. Bresser, D., Buchholz, D., Moretti, A., Varzi, A., and Passerini, S. (2018). Alternative binders for sustainable electrochemical energy storage – the transition to aqueous electrode processing and bio-derived polymers. Energy Environ. Sci. *11*, 3096–3127. https://doi.org/10.1039/C8EE00640G.

41. Hansen, C.M. (2007). Hansen Solubility Parameters: A User's Handbook, Second Edition 2nd ed. (CRC Press). https://doi.org/10.1201/9781420006834.

42. Bottino, A., Capannelli, G., Munari, S., and Turturro, A. (1988). Solubility parameters of

poly(vinylidene fluoride). J. Polym. Sci. B Polym. Phys. *26*, 785–794. https://doi.org/10.1002/polb.1988.090260405.

43. PubChem Ethanol. https://pubchem.ncbi.nlm.nih.gov/compound/702.

44. Yuan, S., Zou, C., Yin, H., Chen, Z., and Yang, W. (2015). Study on the separation of binary azeotropic mixtures by continuous extractive distillation. Chem. Eng. Res. Des. *93*, 113–119. https://doi.org/10.1016/j.cherd.2014.05.005.

45. Chau, J., and Sirkar, K.K. (2021). Organic solvent mixture separation during reverse osmosis and nanofiltration by a perfluorodioxole copolymer membrane. J. Membr. Sci. *618*, 118663. https://doi.org/10.1016/j.memsci.2020.118663.

46. Wang, B., and Lai, Z. (2012). Finger-like voids induced by viscous fingering during phase inversion of alumina/PES/NMP suspensions. J. Membr. Sci. *405–406*, 275–283. https://doi.org/10.1016/j.memsci.2012.03.020.

47. Montina, T., Wormald, P., and Hazendonk, P. (2012). 13C Solid-State NMR of the Mobile Phase of Poly(vinylidene fluoride). Macromolecules *45*, 6002–6007. https://doi.org/10.1021/ma3013477.

48. Moškon, J., Žuntar, J., Talian, S.D., Dominko, R., and Gaberšček, M. (2020). A Powerful Transmission Line Model for Analysis of Impedance of Insertion Battery Cells: A Case Study on the NMC-Li System. J. Electrochem. Soc. *167*, 140539. https://doi.org/10.1149/1945-7111/abc769.J.

49. Landesfeind, J., Hattendorff, J., Ehrl, A., Wall, W.A., and Gasteiger, H.A. (2016). Tortuosity Determination of Battery Electrodes and Separators by Impedance Spectroscopy. J. Electrochem. Soc. *163*, A1373–A1387. https://doi.org/10.1149/2.1141607jes.

50. Pouraghajan, F., Knight, H., Wray, M., Mazzeo, B., Subbaraman, R., Christensen, J., and Wheeler, D. (2018). Quantifying Tortuosity of Porous Li-Ion Battery Electrodes: Comparing Polarization-Interrupt and Blocking-Electrolyte Methods. J. Electrochem. Soc. *165*, A2644–A2653. https://doi.org/10.1149/2.0611811jes.

51. Morasch, R., Landesfeind, J., Suthar, B., and Gasteiger, H.A. (2018). Detection of Binder Gradients Using Impedance Spectroscopy and Their Influence on the Tortuosity of Li-Ion Battery Graphite Electrodes. J. Electrochem. Soc. *165*, A3459–A3467. https://doi.org/10.1149/2.1021814jes.

52. Shodiev, A., Primo, E.N., Chouchane, M., Lombardo, T., Ngandjong, A.C., Rucci, A., and Franco, A.A. (2020). 4D-resolved physical model for Electrochemical Impedance Spectroscopy of Li(Ni1-x-yMnxCoy)O2-based cathodes in symmetric cells: Consequences in tortuosity calculations. J. Power Sources *454*, 227871. https://doi.org/10.1016/j.jpowsour.2020.227871.

53. Doyle, M., Fuller, T.F., and Newman, J. (1993). Modeling of Galvanostatic Charge and Discharge of the Lithium/Polymer/Insertion Cell. J. Electrochem. Soc. *140*, 1526–1533. https://doi.org/10.1149/1.2221597.

54. Fuller, T.F., Doyle, M., and Newman, J. (1994). Simulation and Optimization of the Dual Lithium Ion Insertion Cell. J. Electrochem. Soc. *141*, 1–10. https://doi.org/10.1149/1.2054684.

55. Ferguson, T.R., and Bazant, M.Z. (2012). Nonequilibrium Thermodynamics of Porous Electrodes. J. Electrochem. Soc. *159*, A1967–A1985. https://doi.org/10.1149/2.048212jes.

56. Vasileiadis, A., de Klerk, N.J.J., Smith, R.B., Ganapathy, S., Harks, P.P.R.M.L., Bazant, M.Z., and Wagemaker, M. (2018). Toward Optimal Performance and In-Depth Understanding of Spinel Li 4 Ti 5 O 12 Electrodes through Phase Field Modeling. Adv. Funct. Mater. *28*, 1705992. https://doi.org/10.1002/adfm.201705992.

57. Ombrini, P., Bazant, M.Z., Wagemaker, M., and Vasileiadis, A. (2023). Thermodynamics of multi-sublattice battery active materials: from an extended regular solution theory to a phase-field model of LiMnyFe1-yPO4. npj Comput. Mater. *9*, 148. https://doi.org/10.1038/s41524-023-01109-1.

58. Schwietert, T.K., Ombrini, P., Ootes, L.S., Oostrum, L., Azizi, V., Cogswell, D., Zhu, J., Bazant, M.Z., Wagemaker, M., and Vasileiadis, A. (2023). Phase-Field Computational Framework for Addressing Challenges in Solid-State Batteries. PRX Energy *2*, 033014. https://doi.org/10.1103/PRXEnergy.2.033014.

59. Galuppini, G., Berliner, M.D., Cogswell, D.A., Zhuang, D., Bazant, M.Z., and Braatz, R.D. (2023). Nonlinear identifiability analysis of Multiphase Porous Electrode Theory-based battery models: A Lithium Iron Phosphate case study. J. Power Sources *573*, 233009. https://doi.org/10.1016/j.jpowsour.2023.233009.

60. Sulzer, V., Marquis, S.G., Timms, R., Robinson, M., and Chapman, S.J. (2021). Python Battery Mathematical Modelling (PyBaMM). J. Open Res. Software *9*, 14. https://doi.org/10.5334/jors.309.

61. Andersson, M., Streb, M., Ko, J.Y., Löfqvist Klass, V., Klett, M., Ekström, H., Johansson, M., and Lindbergh, G. (2022). Parametrization of physics-based battery models from input–output data: A review of methodology and current research. J. Power Sources *521*, 230859. https://doi.org/10.1016/j.jpowsour.2021.230859.

62. Wang, A.A., O'Kane, S.E.J., Brosa Planella, F., Houx, J.L., O'Regan, K., Zyskin, M., Edge, J., Monroe, C.W., Cooper, S.J., Howey, D.A., et al. (2022). Review of parameterisation and a novel database (LiionDB) for continuum Li-ion battery models. Prog. Energy *4*, 032004. https://doi.org/10.1088/2516-1083/ac692c.

63. Wang, Q., Zhao, C., Yao, Z., Wang, J., Wu, F., Kumar, S.G.H., Ganapathy, S., Eustace, S., Bai, X., Li, B., et al. (2023). Entropy-Driven Liquid Electrolytes for Lithium Batteries. Adv. Mater. *35*, 2210677. https://doi.org/10.1002/adma.202210677.

64. Wang, Q., Zhao, C., Wang, J., Yao, Z., Wang, S., Kumar, S.G.H., Ganapathy, S., Eustace, S., Bai, X., Li, B., and Wagemaker, M. (2023). High entropy liquid electrolytes for lithium batteries. Nat. Commun. *14*, 440. https://doi.org/10.1038/s41467-023-36075-1.

65. Louli, A.J., Eldesoky, A., Weber, R., Genovese, M., Coon, M., deGooyer, J., Deng, Z., White, R.T., Lee, J., Rodgers, T., et al. (2020). Diagnosing and correcting anode-free cell failure via electrolyte and morphological analysis. Nat. Energy *5*, 693–702. https://doi.org/10.1038/s41560-020-0668-8.

66. Standard Test Methods for Vulcanized Rubber and Thermoplastic Elastomers—Tension https://www.astm.org/d0412-16r21.html.

67. Ogihara, N., Kawauchi, S., Okuda, C., Itou, Y., Takeuchi, Y., and Ukyo, Y. (2012). Theoretical and Experimental Analysis of Porous Electrodes for Lithium-Ion Batteries by Electrochemical Impedance Spectroscopy Using a Symmetric Cell. J. Electrochem. Soc. *159*, A1034–A1039. https://doi.org/10.1149/2.057207jes.

68. Smith, R.B., and Bazant, M.Z. (2017). Multiphase Porous Electrode Theory. J. Electrochem. Soc. *164*, E3291–E3310. https://doi.org/10.1149/2.0171711jes.

69. Doyle, M., Fuller, T.F., and Newman, J. (1993). Modeling of Galvanostatic Charge and Discharge of the Lithium/Polymer/Insertion Cell. J. Electrochem. Soc. *140*, 1526–1533. https://doi.org/10.1149/1.2221597.

70. Balu, B., and Khair, A.S. (2018). Role of Stefan–Maxwell fluxes in the dynamics of concentrated electrolytes. Soft Matter *14*, 8267–8275. https://doi.org/10.1039/C8SM01222A.

71. Nyman, A., Behm, M., and Lindbergh, G. (2008). Electrochemical characterisation and modelling of the mass transport phenomena in LiPF6–EC–EMC electrolyte. Electrochim. Acta *53*, 6356–6365. https://doi.org/10.1016/j.electacta.2008.04.023.

72. McClelland, I., Booth, S.G., Anthonisamy, N.N., Middlemiss, L.A., Pérez, G.E., Cussen, E.J., Baker, P.J., and Cussen, S.A. (2023). Direct Observation of Dynamic Lithium Diffusion Behavior in Nickel-Rich, $LiNi_{0.8}Mn_{0.1}Co_{0.1}O_2$ (NMC811) Cathodes Using *Operando* Muon Spectroscopy. Chem. Mater. *35*, 4149–4158. https://doi.org/10.1021/acs.chemmater.2c03834.